

GRADIENT-FREE AERODYNAMIC OPTIMIZATION WITH STRUCTURAL CONSTRAINTS AND SURGE LINE CONTROL FOR RADIAL COMPRESSOR STAGE

Robert Schaffrath^{1,*}, Eberhard Nicke¹, Nicolai Forsthofer², Oliver Kunc², Christian Voß³

¹German Aerospace Center, Institute of Low-Carbon Industrial Processes

²German Aerospace Center, Institute of Structures and Design

³German Aerospace Center, Institute of Propulsion Technology

ABSTRACT

The concept and design of High Temperature Heat Pumps (HTHP) including their components for specific temperature needs is a time consuming and interdisciplinary task. Especially, the design of compressor geometries has a big impact on the overall performance and the initial costs of the system. For this reasoning, in this work an automated aerodynamic gradient-free optimization including structural constraints for the geometry of a radial compressor impeller blade as well as diffuser vane geometry for water steam, that is applied in a reverse Rankine cycle based HTHP, is presented. Objective of the optimization is the isentropic efficiency in the aerodynamic design point (ADP) of the compressor. Constraints for the pressure ratio, mass flow rate and limits for stresses in blade and disk geometry satisfy requirements of the cycle simulation of the whole HTHP system and structural needs. The optimization method is based on evolutionary algorithms and stochastic surrogate models. Additionally, a highly throttled operating point is regarded to achieve an acceptable distance to the surge line. These types of optimization problems are often characterized by lots of unconverged iterations due to unstable computational fluid dynamic simulations (CFD). To encounter this, a study of the optimization process with different surrogate models is presented. The results are discussed with respect to convergence history as well as objective and constraint improvement.

Keywords: radial compressor, aero-structure optimization, water steam

NOMENCLATURE

Abbreviations

HTHP High Temperature Heat Pump
COP Coefficient of performance
CFD Computational fluid mechanics
CSM Computational structure mechanics

AHPT Automatic hyperparameter tuning
RANS Reynolds-averaged Navier-stokes equation
GCI Grid convergence index
AR Asymptotic range
ADP Aerodynamic design point
HTOP Highly throttled operating point
E Expected improvement
P Prediction minimization
N Neural gas

Roman letters

S Meridional length [–]
m Meridional coordinate [–]
M Mach number [–]
m' Normalized meridional coordinate [–]
n Rotational speed [$\frac{1}{min}$]
r Radial coordinate [*m*]
r Refinement ratio [–]
p Order of convergence [–]
E Discretization error [–]
h Spatial discretization [–]
w_E Weight of Expected improvement [–]
w_P Weight of Prediction minimization [–]
w_N Weight of Neural gas [–]
ṁ Mass flow rate [$\frac{kg}{s}$]

Greek letters

β Beta angle of blade [°]
 θ Circumferential coordinate [°]
 γ Rake angle [°]
 π Pressure ratio [–]
 η Isentropic efficiency [%]
 σ Von Mises stress [*MPa*]

Superscripts and subscripts

tt Total to total property
ts Total to static property

*Corresponding author: robert.schaffrath@dlr.de

1. INTRODUCTION

Global warming is one of the key challenges of the 21st century with wide ranging impact on ecosystems as well as human systems [1]. Especially, the industrial sector is responsible for almost 25% of green house gas emissions. Besides reducing the usage of primary energy sources, the reuse of waste heat is a key for achieving reduction targets. The investigation of high temperature heat pumps (HTHP) is a promising approach to achieve a leap-frogging step in the decarbonization of industrial processes. One of the key components of a high temperature heat pump is the compressor. In many heat pump systems with heat sink temperatures below 100 °C, displacement compressor systems are used. However, turbocompressors are promising alternatives due to higher efficiencies and the ability to operate at high pressure ratios [2, 3]. Especially for the application of heat pump systems in industrial processes, the demand for optimized compressors is rising. In case of medium-sized systems, centrifugal compressors are suitable due to higher pressure ratios and lower mass flow rates (Cordier diagram, [4]).

The optimization of a radial compressor is an interdisciplinary task because of aerodynamic and structural-mechanical requirements, manufacturing limitations and demands on acceptable operating range. Furthermore, the aerodynamic evaluation of compressor geometries with CFD methods is very time-consuming, thus high performance computing systems are needed.

Besides the operating efficiency, the pressure ratio requirements for the specific application defines the design objectives of turbocompressors. Because of that, lots of optimization problems are either constrained by pressure ratio limitations or the pressure ratio is one of the objectives. This leads to shifted aerodynamic design points near the surge line in the performance map of the compressor. To encounter this, different strategies can be found in the literature. A common way is to regard a highly throttled operating point (HTOP) near the surge line during the optimization [5, 6]. By using that operating point, it is possible to define the Cumpsty margin, which is a measure for the distance between the ADP and the surge line. This can be used during the optimization to generate geometries that have a specific distance to the surge line [7]. Otherwise, if the distance is not directly necessary, the highly throttled operating point achieve optimization results that are not located at unstable operating conditions. Another approach is presented by J. Ratz et al. by using local flow parameters to define an objective function for the surge margin, that does not need a highly throttled operating point during the optimization [8]. The advantage is a more stable optimization process, but the initial computational cost is higher, because of preliminary surge line calculations. It could be shown, that the optimization result with an objective function based on flow parameters is comparable to a common approach with a highly throttled operating point. Similar suggestions can be found in [9, 10].

The elevated number of optimization parameters of the compressor geometry require an automated optimization process. Gradient-based and gradient-free methods could be successfully applied on radial compressor optimization tasks [11–13]. The advantage of gradient-free methods is that they are suitable to reach a global optimum and can handle non-differentiable objec-

tives and even unconverged simulations, but suffer by the number of objective evaluations. In contrast, the gradient-based methods require less objective evaluations because of information of steepest descent, but most likely will converge to a local minimum. In their work Hottois et al. showed by applying a gradient-free and a gradient-based optimization on a turbine vane that both methods reveal similar results [14]. Nevertheless, their findings also prove that gradient-based methods can reach the global optimum in case of highly complex optimization problems. For acceleration of gradient-free methods, surrogate models are commonly used [12, 13, 15]. The general idea of a surrogate model is to use information based on already successfully calculated compressor geometries and create a fast to evaluate mathematical function for the objective. Now the algorithm can be used to run the optimization with the surrogate model instead of the complex and exact compressor evaluation. Nowadays, Kriging-based methods (also known as Gaussian process regression) are frequently used as surrogate model. The Kriging surrogate model can be evaluated in different ways. The most common infill criterion is expected improvement and prediction minimization, which is also known as volume gain in the literature. A third way is entropy maximization, but this is a less frequent application of that method, because of the very explorative character and so it is used effectively only in the beginning of an optimization. Another surrogate model is neural gas, based on self-organizing maps, that can be used to predict well performing geometries. Further information can be found in [16], [17] and [18].

During an optimization it is possible to use different infill criteria. In the literature, we could found only one publication with such an optimization methodology [16]. M. H. Aissa and T. Verstraete presented a gradient-free aero-structure optimization with alternating infill criteria with expected improvement and prediction minimization. The application was a radial compressor impeller geometry. But so far, to the best knowledge of the authors, a comprehensive study to different infill criteria during an aerodynamic optimization with the goal of finding optimal combinations is an innovative investigation. Probable causes are on the one hand side the enormous amount of cluster contingent to run an optimization multiple times with different infill criteria and on the other hand the sparse availability of different surrogate models implemented in the used design suites.

The structure of the paper is as follows: the following section presents the optimization methodology and the parametrization of the compressor geometry. Furthermore, details of the meshing process, CFD calculations, computational structure mechanics (CSM) calculations and post-processing of the data will be presented. The third section gives an overview of the applied surrogate models and infill criteria. The next section presents the optimization results. This is followed by comparing the baseline and optimised geometry. Finally, an automatic hyperparameter tuning (AHPT) is carried out.

2. OPTIMIZATION METHODOLOGY

For solving the optimization problem, AutoOpti is used, see i.e. [12, 19]. It implements a gradient-free evolutionary algorithm accelerated with different surrogate models and infill criteria. The evaluation of geometries during each iteration step

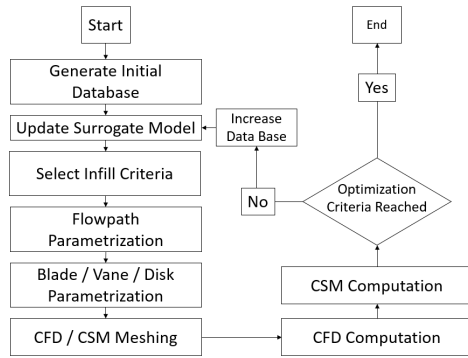


FIGURE 1: SCHEMATIC OVERVIEW OF OPTIMIZATION METHODOLOGY

is enabled by a user defined process chain. AutoOpti is highly parallelized by multiple process chain evaluations at the same time, with the goal of fast optimization convergence. The general optimization procedure is shown in Fig. 1. The optimization is initiated with a randomly generated database, followed by the training of surrogate models. Surrogate models that are implemented in AutoOpti are for example Kriging approximation and neural gas. Furthermore, infill criteria implemented for Kriging approximation are expected improvement and prediction minimization. An overview of the surrogate models and criteria will be given in section 3. After successful training of surrogate models, an infill criterion is selected, which is subsequently implemented by randomized selection with user defined probabilities for each infill criteria. By using that procedure, it is possible to combine exploitative and explorative system behaviour. The next steps describe the geometry parametrization of the impeller and diffuser and CFD as well as CSM evaluation. Details are given in subsection 2.1. After successful process chain evaluations, the convergence criteria are checked. We are using a maximum number of successful process chain evaluations and a time limit for terminating the optimization process.

2.1 Parametrization

The first step of the geometry parametrization is the flow path, that is designed by a hub and shroud curve in the meridional plane, see Fig 2. Impeller and diffuser are located inside the flow path and are visualized with a black mesh. In order to modify the flow path of the compressor, the hub and shroud curve are splined by control points. The first and second control points for the shroud curve are used to modify the impeller inlet diameter. The first free variable #1 is used for both control points to achieve a straight inlet, by modifying the radial component. The next three control points are individually shifted in the normal direction from hub to shroud by free variables #2 - #4. Because of the big influence of the flow path along the impeller length of the ADP, three control points are used. For simplifying the manufacturing of the diffuser area, a constant shroud contour is preferred. For the realization, six control points are included with an axial degree of freedom, that are controlled by free variable #5. In contrast, the hub curve is only parametrized by one free variable #6, because of the reduction of free variables. The location of control point

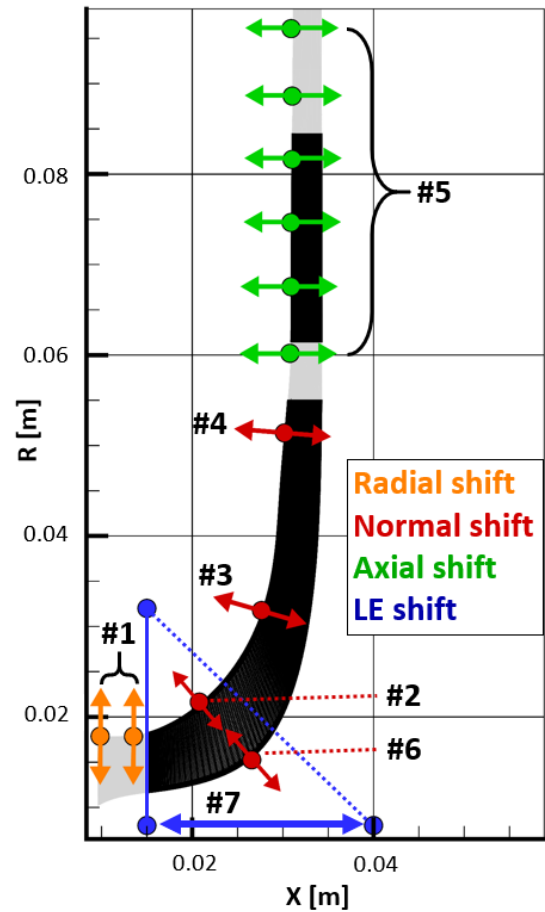


FIGURE 2: PARAMETRIZATION OF FLOW PATH IN MERIDIONAL PLANE

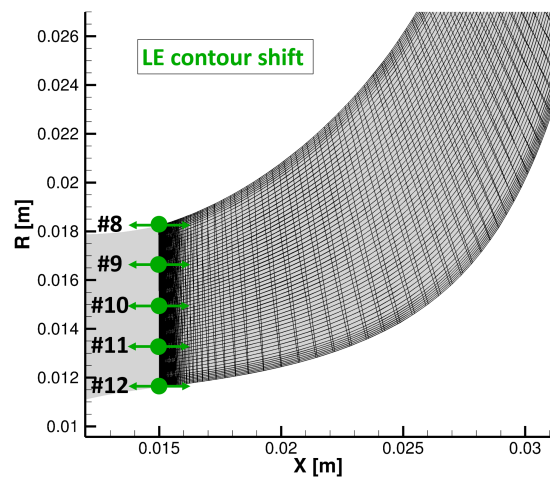


FIGURE 3: PARAMETRIZATION OF LEADING EDGE CONTOUR BY CONTROL POINTS IN MERIDIONAL PLANE

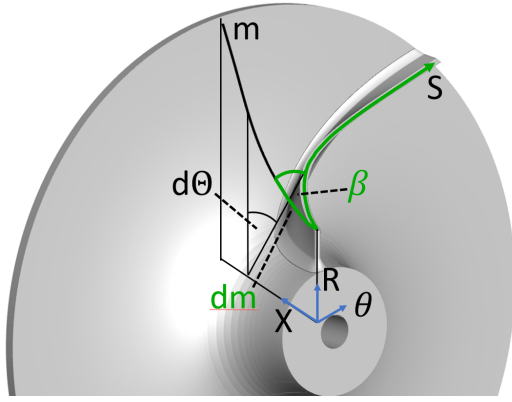


FIGURE 4: DEFINITION OF β AND θ ANGLE

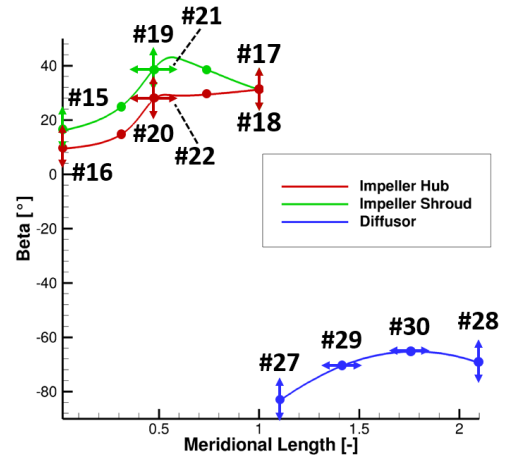


FIGURE 5: β ANGLE DISTRIBUTION OF BLADE AND VANE IN MERIDIONAL PLANE

is within the area of highest curvature, because of the biggest influence in aero- and structural mechanics and can be shifted in orthogonal direction to the hub curve.

With defined flow path shifts, the parametrization of blade and vane can be conducted. The first step is the parametrization of the leading edge of the blade, see Fig. 3. In the literature, comparable radial compressor impeller optimization have shown, that huge geometry modifications of the leading edge can occur during an automated optimization [6, 12]. Because of that, five equally distributed control points for the parametrization of the leading edge are used. For each of these control points, a free variable #8 - #12 for the axial shift is applied. Furthermore, an overall shift in the meridional plane of the leading edge is regarded by free variable #7, by modifying the slope of the blue dashed line, see Fig. 2. By using that scheme, the limit of free variables #8 - #12 can be reduced, due to the overall shift by free variable #7. This kind of scheme should result in a more stable blade parametrization.

The shape of the blade camber line is designed by a distribution of β angle in (m', θ) coordinate system. The angle β is defined as the angle between the meridional plane and S , that is calculated by integration of ds , which is:

$$ds = \sqrt{(dx)^2 + (dr)^2 + (rd\theta)^2} \quad (1)$$

The meridional plane is defined by the arc length

$$dm = \sqrt{(dx)^2 + (dr)^2} \quad (2)$$

and m' can be defined as differential normalized arc length with respect to the impeller radius r in the meridional plane by

$$dm' = \frac{dm}{r} \quad (3)$$

With the notation defined previously, the β angle can be defined as

$$\tan \beta = \frac{rd\theta}{dm} \quad (4)$$

The definition of β , S , m and θ can be seen in Fig. 4. Further information can be found in [4, p. 467] and [20].

Because of prescribed notations, it is sufficient to define the β angle distribution in (m', θ) coordinate system. Furthermore,

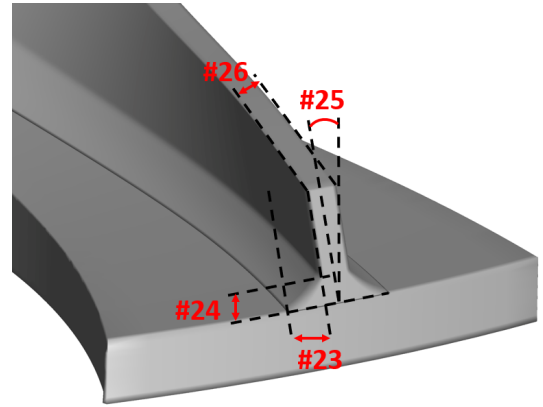


FIGURE 6: DEFINITION OF RAKE ANGLE γ , LOWER BLADE THICKNESS AND FILLET STRUCTURE

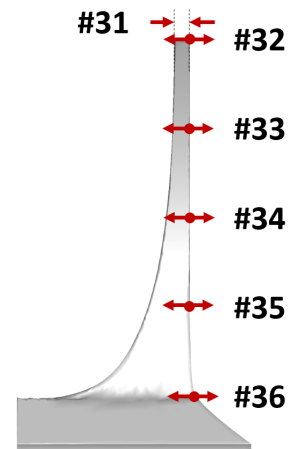


FIGURE 7: PARAMETRIZATION OF REAR SIDE OF DISK

the circumferential coordinate θ has to be defined. The blade is defined by two profiles along the span, one located at the hub and the second at the shroud contour. The vane is constant in spanwise direction, in order to reduce the number of free variables. Due to the strong impact of the blade to the overall compressor performance, more free variables are defined for parametrization. The circumferential coordinate for the hub profile of the blade is defined as free variable #13, the shroud profile is free variable #14 and the vane profile is free variable #40. For each profile, the β angle distribution can be seen in Fig. 5. The shape of the profile is parametrized by control points. The profiles of the blade consist of 5 and the profile of the vane consist of 4 control points, respectively. The blade β angle at the leading edge is parametrized by free variable #15 and #16 and at the trailing edge by free variable #17 and #18 for hub and shroud profile. The meridional coordinate of the second and fourth control point is fixed and the β angle is being derived by the β angle at the leading and trailing edge, respectively, because of continuous and differentiable condition of the overall profile shape. The meridional coordinate and β angle of the third control point is parametrized for both profiles. The β angles are shifted by free variables #19 and #20 and the meridional coordinate by free variables #21 and #22 in case of hub and shroud profile. The choice of the control points and the degrees of freedom is a good compromise between reduction of the number of free variables and variability of the blade parametrization. The β angle of the leading and trailing edge of the vane is parametrized by free variable #27 and free variable #28 respectively. The intermediate control points are located at 33 % and 66 % of vane meridional length. The only degree of freedom is described by the meridional coordinates of the control points, that are parametrized by free variable #29 and #30. Furthermore, blades and vanes that are defined by multiple control points result in wavy geometries with high manufacturing costs.

The definition of the rake angle, the free variables of the fillet parametrization and the thickness of the impeller blade can be seen in Fig. 6. The rake angle is defined by the positive angle between the line, that connects the trailing edge points of both design profiles and the vertical line that intersects the hub profile at the trailing edge location. The rake angle is controlled by the circumferential shift of the shroud profile with free variable #25. The thickness of the blade at the leading edge is kept constant at 1.3 mm. To satisfy structural-mechanical requirements, the blade thickness at the trailing edge position is parametrized by free variable #26. The intermediate thickness is linearly interpolated between the leading and trailing edge. The fillet is designed by two free variables. The first free variable #23 controls the blow curve that is the increased profile at the hub surface, where the smooth connection between blade and disk starts. The blade curve, that is an intermediate profile between hub and shroud profile, is designed by free variable #24. Based on these two profiles, the fillet is designed as a slightly smoothed curve between them. A perfect circular fillet could not be used, since the fillet radii are lower than 1 mm, which results in hard to manufacture geometries. The free parameters for fillet design can be seen in Fig. 6.

To satisfy structural-mechanical requirements, it is not only suf-

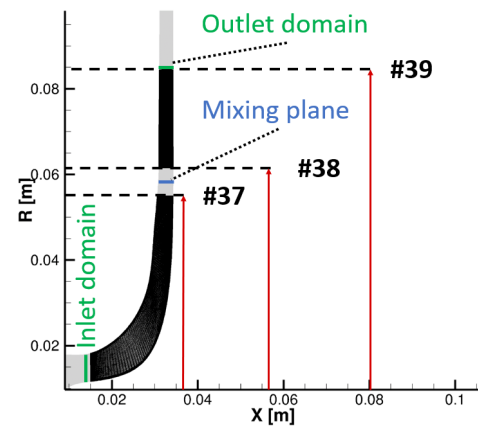


FIGURE 8: DEFINITION OF DIAMETERS OF IMPELLER AND DIFFUSOR

ficient to consider the blade, but also the disk geometry of the radial compressor. The parametrization of the disk is shown in Fig. 7. The overall thickness of the disk is designed by free variable #31. Intermediate shifts of the rear side according to x direction are controlled by free variables #32 - #36. The shift locations start at the radius of the trailing edge of the blade and end at the radius of the leading edge.

Furthermore, the general radii of impeller and diffuser are considered. The parametrization can be seen in Fig. 8. The impeller radius is controlled by free variable #37, the vaneless space by free variable #38 and the radius of the diffuser by free variable #39. Additionally, a constraint is regarded that the vaneless space is always positive and at least 5 mm. Moreover, the location of the mixing plane is always shifted in the middle of the vaneless space. In the same way, the outlet domain is moved right behind the trailing edge.

All of the parametrization of blade geometry is done with the DLR internal tool *BladeGenerator*. The number of blades is being kept at 19 and the number of vanes at 14. For more information see [19].

2.2 CFD Mesh generation and grid convergence

For evaluation of compressor performance, a CFD calculation of impeller and diffuser geometry is carried out. Based on the parametrized geometry, the CFD mesh is computed by using a DLR internal meshing tool PyMesh [21]. It implements an O-C-H mesh topology, with shape modifications done by cell spacings, block relationships and dimensions. Because of the coupled rotor-stator computation, two individual meshes are calculated. The connection is done at the mixing plane, see Fig. 8. In order to run low-reynolds CFD models, the mesh was iteratively refined. The evaluated y^+ values at boundaries are below 1. An exception is the tip clearance of the impeller geometry, where wall functions are used in order to reduce the mesh dimension. The complete compressor mesh is visualized in Fig. 9 and a detail view of the leading edge mesh is shown in Fig. 10. Both visualizations show the mesh at 50% span.

For proofing the mesh resolution, a grid convergence study is

TABLE 1: RESULTS OF GRID CONVERGENCE STUDY FOR RADIAL COMPRESSOR STAGE

	# Cells	π_{ts} [-]	η_{tt} [%]	Rel. Error π_{ts}	Rel. Error η_{tt}
Coarse Grid	580.944	1,97294	0,68261	0,000968	0,006947
Medium Grid	883.932	1,97594	0,67644	0,000553	0,002156
Fine Grid	1.413.027	1,97514	0,67762	0,000147	0,000413
Richardson Extra.		1,97485	0,67790	0	0

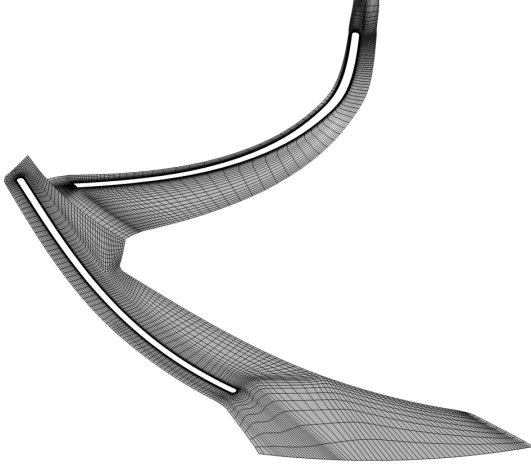


FIGURE 9: FINEST MESH OF IMPELLER AND DIFFUSER AT MIDSPAN

carried out. Therefore, the mesh was coarsened two times with a refinement ratio r of approximately 1.2 in every dimension. The process was done by adapting the major block dimensions and constant near boundary cell spacing to enable successful simulation without the necessity of wall functions, except the tip clearance. Based on the fact, that only integer numbers of block dimensions are modified, the theoretical refinement ratio of 1.2 could not be reached exactly at some mesh modifications. The CFD simulation is solved on every mesh.

In order to compare the results to a theoretical on an infinitesimal fine mesh, the method of Richardson extrapolation is applied. The theory behind the Richardson extrapolation can be described by the relation $E = C * h^p$, where E is the error, p is the convergence order and h is spatial discretization. By applying Taylor approximation, the value of the computed parameter on an infinitesimal fine mesh can be calculated by equation 5

$$f_{h=0} = f_{\text{fine}} + \frac{f_{\text{fine}} - f_{\text{medium}}}{r^p - 1}. \quad (5)$$

The calculation of p can be seen in equation 6.

$$p = \frac{\ln\left(\frac{f_{\text{coarse}} - f_{\text{medium}}}{f_{\text{medium}} - f_{\text{fine}}}\right)}{\ln(r)} \quad (6)$$

By the help of the Richardson extrapolation, the error between every solved mesh and the solution on theoretical infinitesimal fine mesh can be calculated. After that, the grid convergence index (GCI), which is a measure to display the grid quality, can

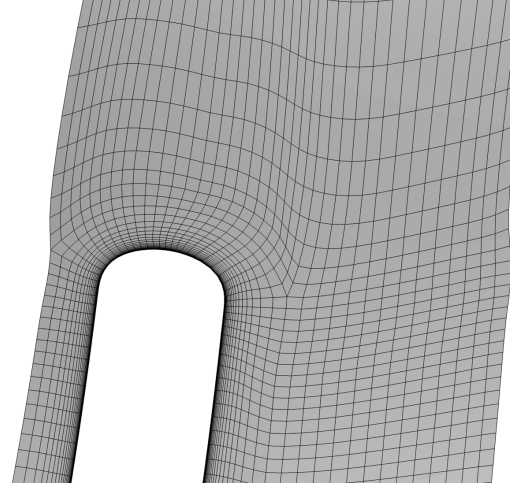


FIGURE 10: FINEST MESH OF IMPELLER LEADING EDGE AT MIDSPAN

be calculated for refinement steps from *coarse* to *medium* and *medium* to *fine* by

$$GCI_{\text{coarse,medium}} = \frac{F_s * \epsilon_{\text{coarse,medium}}}{r^p - 1} \quad (7)$$

and

$$GCI_{\text{medium,fine}} = \frac{F_s * \epsilon_{\text{medium,fine}}}{r^p - 1} \quad (8)$$

with F_s as safety factor, which is usually around 1.25 and $\epsilon_{\text{coarse,medium}}$ and $\epsilon_{\text{medium,fine}}$ are the relative errors between coarse and medium and medium and fine grid, respectively. Finally, it is possible to ensure, that all grids are in asymptotic range (AR). That can be done by calculating

$$AR = \frac{GCI_{\text{coarse,medium}}}{r^p * GCI_{\text{medium,fine}}}. \quad (9)$$

For AR, equation 9 has to be close to 1.0. The results of the CFD calculations for isentropic efficiency η_{tt} and total to static pressure ratio π_{ts} on every mesh as well as the results of the Richardson extrapolation can be seen in Table 1. Furthermore, the relative error for η_{tt} and π_{ts} between Richardson extrapolation and mesh solution is plotted in Fig. 11. The error of η_{tt} is higher for coarse meshes compared to the error of π_{ts} , because of the more complex structure and dependencies of the efficiency definition. The corresponding asymptotic ranges are 0.99959 in case of π_{ts} and 1.0017 for η_{tt} . Further information on the Richardson extrapolation and grid convergence studies can be found in [22] and [23]. For the optimization, the finest mesh was used.

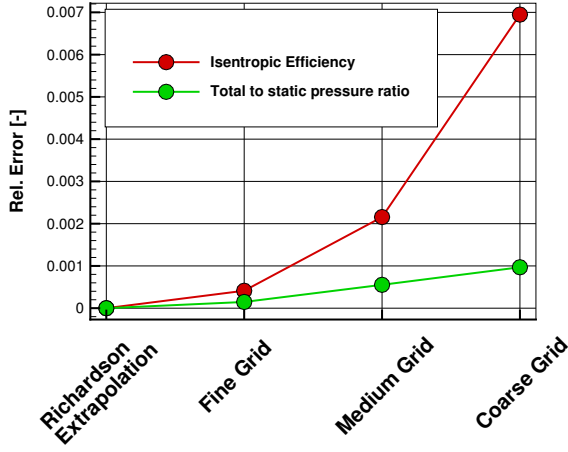


FIGURE 11: RELATIVE ERRORS BETWEEN DIFFERENT MESH RESOLUTIONS AND RICHARDSON EXTRAPOLATION

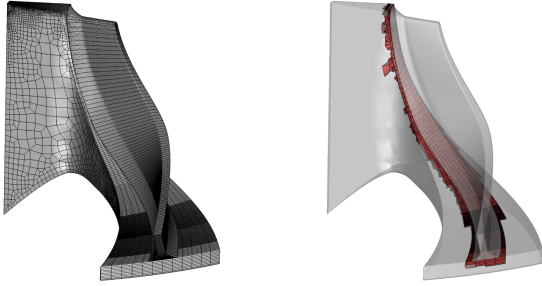


FIGURE 12: CSM MESH FOR BLADE AND DISK (LEFT) AND IGNORED CELLS (RED) IN STRESS POST PROCESSING (RIGHT)

2.3 CFD simulation

The performance of the radial compressor stage is carried out by CFD calculation of steady state Reynolds-averaged Navier-Stokes equation (RANS). The inlet and outlet domain can be seen in Fig. 8. Because of the periodicity of the geometry, only one segment is calculated. Therefore, a mixing plane is used between the rotating and stationary stage. For the calculation of the thermodynamic properties of water steam, the ideal gas model is applied. The viscosity is calculated by using the Sutherland model. The influence of the turbulence is considered by Menter SST turbulence model. The solver is back-pressure controlled and a second order spatial discretization scheme is used. At the compressor inlet, the stagnation pressure and stagnation temperature and at the outlet the static pressure are defined, respectively. For successful convergence, the variation of mass flow rate, pressure ratio and isentropic efficiency between inlet and outlet have to be smaller than 0.0005 for 200 time steps. The calculation is initialized by a circumferential averaged solution of the baseline geometry. The simulation is conducted by using the solver TRACE [24].

2.4 CSM simulation

For satisfaction of structural-mechanical requirements, a static CSM simulation for the rotating stage is executed. The meshing process is implemented by using a DLR internal mesh-

ing software. The blade and disk geometry are individually discretized by hexahedral mesh and connected by multi-point constraints (MPC). Based on the aerodynamic simulation, the pressure and temperature loads are considered. In addition, the rotation of the geometry is a further mechanical load for the system. By using cyclic boundary conditions, only one blade and disk segment is taken into account. For the solution, the open source solver CALCULIX with compiled solver SPOOLES is applied [25]. Because of the MPC, stresses in the connection area are potentially unreliable. To encounter this, the MPC cells are not taken into account for automatic post-processing during the optimization process. The CSM mesh and the cells, that are neglected in post-processing, are shown in Fig. 12. Besides that, the first 5% of the blade height are neglected to not sophisticate the post-processing process. Preliminary simulations revealed, that the maximum stress values are not located in that region, therefore the limited post-processing has no influence on the final CSM result.

2.5 Objective and constraints

The optimized compressor geometry will be integrated in a HTHP with water steam as working fluid. To achieve a high temperature lift, the heat pump consists of three compressor stages. The goal of the presented optimization methodology is to maximize the efficiency in the ADP of the second stage. Because of already existing performance maps of the first and third stage, constraints for the mass flow rate and the pressure ratio are necessary. The mass flow rate in the ADP should be above $0.175 \frac{\text{kg}}{\text{s}}$ to reach the design criteria of the heat exchangers and below $0.275 \frac{\text{kg}}{\text{s}}$ to satisfy the power consumption limit of the gear system. Furthermore, the pressure ratio of the compressor stage should be above 2.3. The material of rotor and stator will be the titanium alloy Ti-6Al-4V, hence the stresses in the impeller should be below 600 MPa. Besides the ADP, a highly throttled operating point will be regarded, to ensure a decent distance of the ADP to the surge line. That operating point will be at the same speed line, but with an increased back pressure by 2%. During the optimization, no surge margin distance will be calculated, therefore no Cumpsty margin is calculated either. For the highly throttled operating point, only the convergence of CFD is required. The objective will be the maximization of the efficiency in the ADP. The initial design does not satisfy the pressure ratio and structural-mechanical needs and is derived by a design of an already existing compressor test rig. The optimization problem can be formulated as:

$$\begin{aligned}
 \text{Minimize } Obj &\equiv - \frac{\eta_{tt}}{\eta_{tt}^{\text{Baseline}}} \\
 \text{subject to Constraint 1} &\equiv \frac{\dot{m}}{0.25 \frac{\text{kg}}{\text{s}}} \in [0.7, 1.1] \\
 \text{Constraint 2} &\equiv \frac{\pi_{ts}}{2.3} \in [1, \text{inf}] \\
 \text{Constraint 3} &\equiv \frac{\sigma_{mises}}{600} \in [0, 1] \\
 \text{Constraint 4} &\equiv \text{HTOP CFD converged}
 \end{aligned} \tag{10}$$

3. SURROGATE MODELS

Gradient-free optimization approaches suffer from low convergence rates, hence new designs are created by genetic operations like mutation or cross over. To encounter this, surrogate models are used. In this section, three different types of surrogate models are presented at a glance. For detailed explanations, as well as implementation strategies, further references in the literature are given.

A classical and well-known surrogate model is the Gaussian process regression, also known as Kriging. In case of ordinary Kriging, the idea is to approximate the function by the main trend with one regression function combined with a Gaussian random process with zero mean. The covariance of the random process is assumed to be only depended on the distance of two arguments multiplied with a constant variance. The free parameters of the regression function and of the random process are determined, such that the Kriging model is the best linear unbiased predictor. This process is called training of the surrogate model. The result is a surrogate model, that does not only give predictions of function values, but also a value of the variance of the prediction. The variance of the prediction is small in the area of already existing datasets, and increases with increasing distance. Based on that, it is possible to define the different infill criteria. The first and very common approach is called *Expected Improvement* (E). The idea is to scan the surrogate model for arguments with the biggest chance of getting better than the current best dataset in the database. Another infill criteria is called *Prediction Minimization* (P), with the goal in only going to minimize the value of the prediction without consideration of the variance. Further information on Kriging surrogate models can be found in [16] and [17].

Another surrogate model is called *Neural Gas* (N). The idea is to use self-organizing maps, also known as Kohonen net, that is a kind of artificial neural network. Each neuron of the Kohonen net consists of a weight out of the argument set and a position in 2-dimensional space. Higher dimensions are also possible. During the training phase, the weights of the neurons are adapted, such that similar samples are located closer and adjective samples far more apart. New samples are generated through the evaluation of the artificial neural network. Further information on Neural Gas can be found in [18].

4. OPTIMIZATION PROBLEM

The optimization process is started by 100 randomly generated geometries based on the baseline geometry. Next, all of the new iterations are generated by surrogate model evaluations. The rotational speed in the ADP is 100.000 rpm. The inlet condition was defined by a total pressure of 3.8 bar and a total temperature of 420.0 K. The infill criteria is selected by a random process with weight w_E for Expected Improvement, w_P for Prediction Minimization and w_N for Neural Gas. Each weight has to be in $R_+ := [0, \infty)$. The ratio $\frac{w_i}{w_E + w_P + w_N}$ describes the probability of selecting the surrogate model i . A maximum number of 1500 iterations was used for terminating the optimization process.

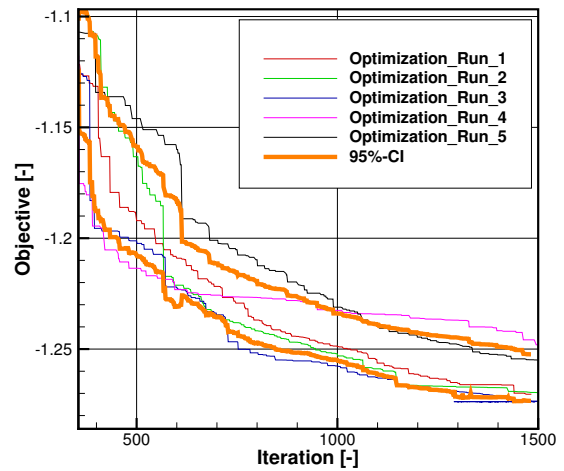


FIGURE 13: COMPARISON OF THREE OPTIMIZATION RUNS WITH SAME INFILL CRITERIA AND CALCULATED 95% CONFIDENCE INTERVAL

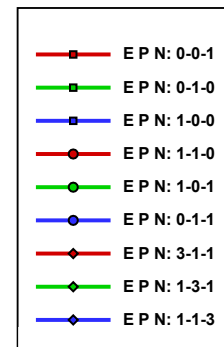
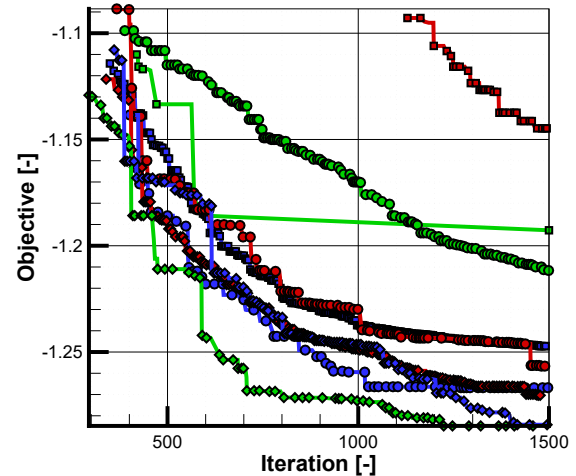


FIGURE 14: CONVERGENCE HISTORY OF DIFFERENT COMBINATIONS OF INFILL CRITERIA AND CONFIDENCE INTERVAL AT 95% LEVEL

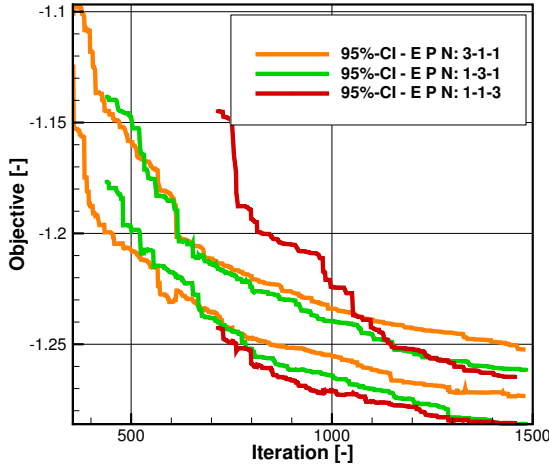


FIGURE 15: COMPARISON OF THREE 95% CONFIDENCE INTERVAL OF INFILL CRITERIA COMBINATIONS

4.1 Optimization results

The first optimization run was conducted with infill criteria probabilities $(w_E, w_P, w_N) = (3, 1, 1)$. Because of the stochastic nature of both the infill criteria selection and the surrogate model structure as well as the evolutionary algorithm for solving the optimization problem, the optimization was repeated five times. The optimization process can be seen in Fig. 13. The figure shows only iterations, that satisfy all of the constraints and have a converged highly throttled operating point. It can be seen, that neither the baseline geometry nor one of the 100 randomly generated members for the initial dataset, are satisfying all of the constraints. Moreover, the first member that fulfills all of the constraints can be found after approximately 300 iterations. Besides the objective decrements, a confidence interval with a 95% level is shown. It can be seen, that the confidence interval is wide in the early phase and narrow in the late phase of the optimization. Possible reasons are the strong dependence of the objective process on the infill criteria selection, which are depending on the selected criteria. During the ongoing optimization, the ratio of the selected infill criteria is converging to the predefined probability distribution, hence the confidence interval is decreasing. Besides that, all objective decrements are not fully converged within the iteration limit. This motivates to investigate different infill criteria probabilities.

The comprehensive study is shown in Fig. 14. The convergence trajectories with only one kind of surrogate model $(w_E, w_P, w_N) = (0, 0, 1)$, $(w_E, w_P, w_N) = (0, 1, 0)$ and $(w_E, w_P, w_N) = (1, 0, 0)$ are shown with squares as symbol, combinations of two different surrogate models $(w_E, w_P, w_N) = (1, 1, 0)$, $(w_E, w_P, w_N) = (1, 0, 1)$ and $(w_E, w_P, w_N) = (0, 1, 1)$ are visualized by circles and those combining three $(w_E, w_P, w_N) = (3, 1, 1)$, $(w_E, w_P, w_N) = (1, 3, 1)$ and $(w_E, w_P, w_N) = (1, 1, 3)$ are plotted using diamonds. No further combinations were conducted. In addition, the confidence interval is shown. It can be seen, that the convergence behaviour

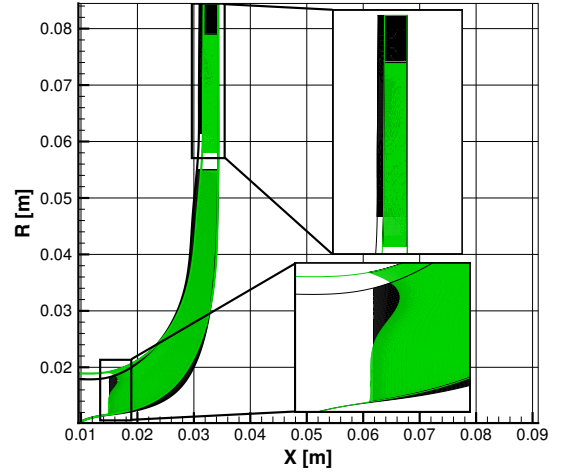


FIGURE 16: BASELINE GEOMETRY (BLACK) AND OPTIMIZED FLOW PATH (GREEN) IN MERIDIONAL PLANE

of only N (red square) is the least optimal. Similar results can be observed for P (green square). Possible reasons are the very exploitative and no explorative strategy of these surrogate models. Only two infill criteria combinations $(w_E, w_P, w_N) = (1, 3, 1)$ (green diamond) and $(w_E, w_P, w_N) = (1, 1, 3)$ (blue diamond) reach the best solution with an objective decrement of -1.285. For both trajectories, a good convergence behaviour can be noticed. The other combinations of surrogate models performing similar to the first investigated combination and are in the area of the confidence interval.

Further statistical comparison of three different infill criteria combinations are shown in Fig. 15. Because of limited cluster contingent, only the combinations $(w_E, w_P, w_N) = (3, 1, 1)$, $(w_E, w_P, w_N) = (1, 3, 1)$ and $(w_E, w_P, w_N) = (1, 1, 3)$ are carried out. Each confidence interval was calculated based on 5 optimizations. It can be clearly seen, that the mean of confidence interval of $(w_E, w_P, w_N) = (1, 1, 3)$ is lower than the means of the other confidence intervals. The least optimal mean has combination $(w_E, w_P, w_N) = (3, 1, 1)$. Furthermore, the width of all three confidence intervals is comparable.

4.2 Result interpretation

The baseline geometry is compared with the last iteration of the optimization run with infill criteria combination $(w_E, w_P, w_N) = (1, 3, 1)$. The geometry is the same as the result of optimization run with infill criteria combination $(w_E, w_P, w_N) = (1, 1, 3)$. The flow path variation and the radial start and end positions of blade and vane can be seen in Fig. 16. Only slight modifications of the flow path can be noticed. The diameter of the impeller nearly kept constant, but the radial starting position of the vane which was decreased by free variable #38: $0.062 \rightarrow 0.0585$ as well as the diameter by free variable #39: $0.084 \rightarrow 0.0788$. The optimizer was able to reach the required pressure ratio without increasing the impeller diameter, which often leads to higher losses due to higher outlet Mach numbers. The decrement of the vaneless space reduces the logarithmic path

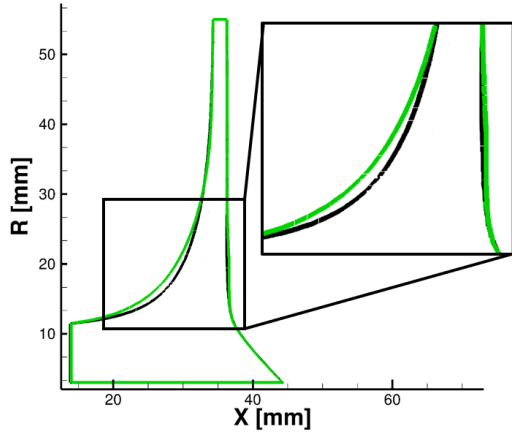


FIGURE 17: BASELINE (BLACK) AND OPTIMIZED (GREEN) DISK GEOMETRY IN THE MERIDIONAL PLANE

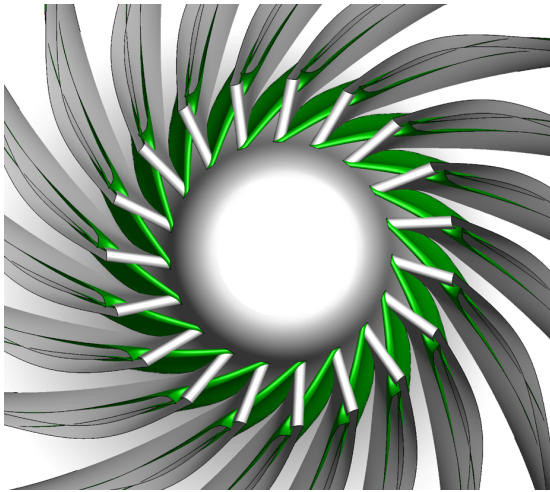


FIGURE 18: COMPARISON OF BASELINE (BLACK) AND OPTIMIZED (GREEN) GEOMETRY WITH FOCUS ON INLET

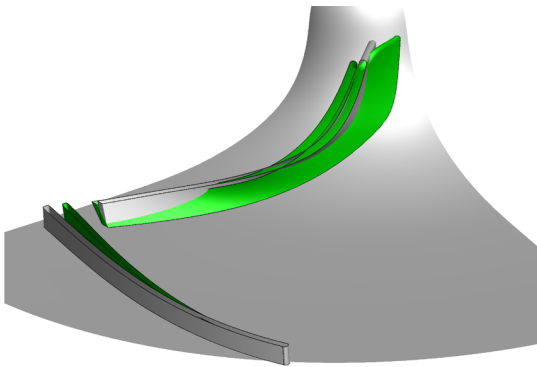


FIGURE 19: SINGLE BLADE AND VANE COMPARISON OF BASELINE (BLACK) AND OPTIMIZED (GREEN) GEOMETRY

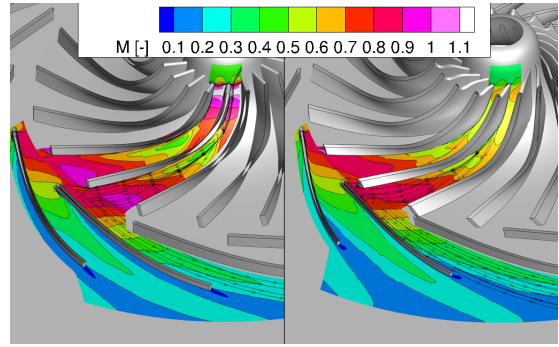


FIGURE 20: FLOW COMPARISON OF ABSOLUTE MACH NUMBER AT 50% SPAN BETWEEN BASELINE (LEFT) AND OPTIMIZED (RIGHT) GEOMETRY

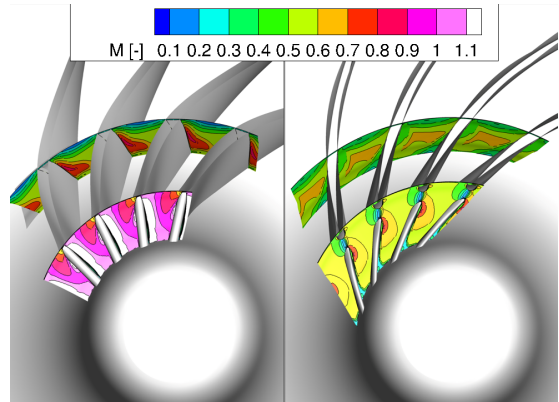


FIGURE 21: COMPARISON OF ABSOLUTE MACH NUMBER IN PASSAGE AT INLET AND INTERMEDIATE POSITION BETWEEN BASELINE (LEFT) AND OPTIMIZED (RIGHT) GEOMETRY

of the fluid behind the impeller caused by the guided stream path by the vaned diffuser. The reduction of the diffuser diameter reduces friction losses. The optimized disk geometry is shown in Fig. 17. Slight modifications in the rear side can be identified by adapting free variable #35: $0 \rightarrow 0.0003$. The overall disk thickness was kept constant.

The blade parametrization was highly modified. Figure 18 and 19 shows the redesigned inlet geometry with modified lean angle and the optimized leading edge contour with a one-sided S-shaped contour. The β angle was increased in case of hub surface by free variable #16: $5^\circ \rightarrow 9.98^\circ$ and for the casing by free variable #15: $15^\circ \rightarrow 19.4^\circ$. The β angles at the trailing edge did not change significantly. The leading edge contour was designed by huge increment of free variable #9: $0 \rightarrow 0.2$, which is the upper limit for the optimizer. With an increased limit, the optimizer would probably select bigger shifts. The shock losses could be significantly avoided by shifting the impeller from a transonic to nearly subsonic behaviour. The β angle of the vane was slightly increased at the leading edge by free variable #27: $-83.5^\circ \rightarrow -82.73^\circ$ and at the trailing edge by free variable #28: $-69.5^\circ \rightarrow -65.3^\circ$. The θ angle was reduced by free variable #40: $160^\circ \rightarrow 157.1^\circ$.

The resulting flow based on the shape modifications can be seen in Fig. 20. The Mach number at 50% span is shown. The flow is successfully decelerated at the inlet and outlet area of the im-

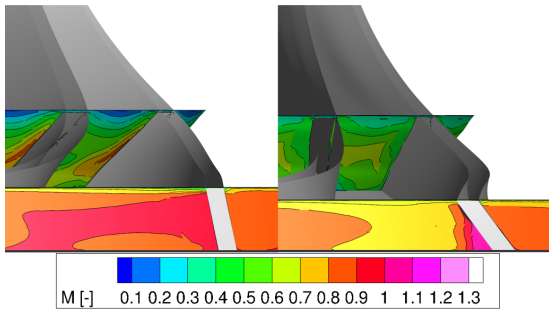


FIGURE 22: COMPARISON OF ABSOLUTE MACH NUMBER IN PASSAGE AT IMPELLER OUTLET BETWEEN BASELINE (LEFT) AND OPTIMIZED (RIGHT) GEOMETRY

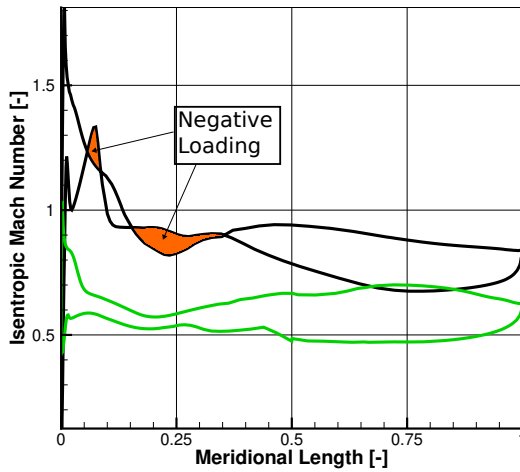


FIGURE 23: COMPARISON OF AERODYNAMIC LOADING OF BASELINE (BLACK) AND OPTIMIZED (GREEN) GEOMETRY AT 50% SPAN

pellor. Additionally, the flow on the suction side is homogenized, which leads to reduced losses due to secondary flow phenomena. The flow in the diffuser passage is kept constant, but with a decreased diffuser diameter, that reduces the friction. A detailed view on the passage flow of the impeller is shown in Fig. 21. It can be seen, that the redesigned lean angle of the leading edge and the complex leading edge contour reduce the Mach number significantly. Again, a detailed view on the flow inside the impeller passage is given, that shows the deceleration of the flow at the suction side, that results in lower flow separation. The comparison of the flow at the outlet of the impeller can be seen in Fig. 22. Due to the optimized rake angle by free variable #25: $0 \rightarrow 0.0276$, the passage flow is reduced, hence the transformation of kinetic energy to static pressure in the diffuser area is improved.

The aerodynamic loading of the impeller blade at 50% span is shown in Fig. 23. The black line shows the isentropic Mach number of the baseline geometry and the loading of the optimized geometry is shown in green. Two highlighted areas can be identified with negative loading of the baseline impeller. The optimized geometry has no areas with negative loading. Furthermore, the overall loading behaviour is homogenized throughout

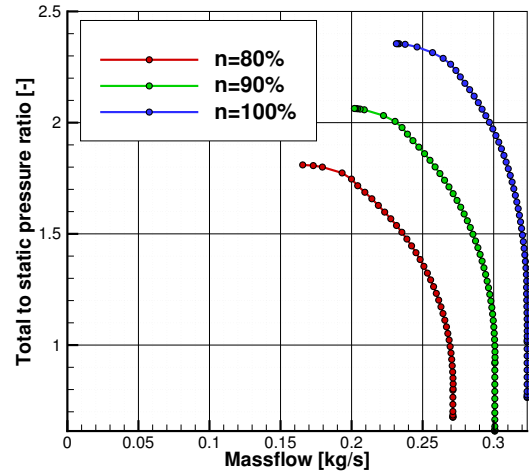


FIGURE 24: PERFORMANCE MAP WITH TOTAL TO STATIC PRESSURE RATIO OF OPTIMIZED GEOMETRY

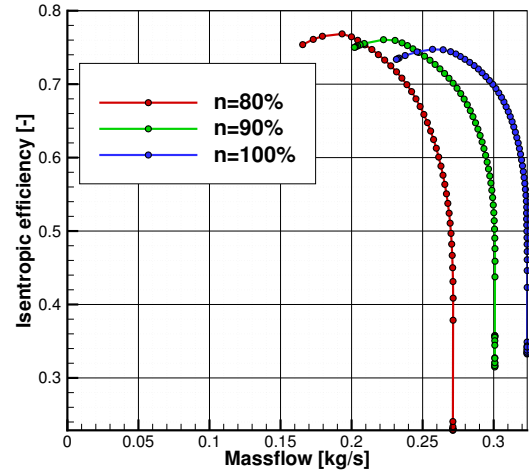


FIGURE 25: PERFORMANCE MAP WITH ISENTROPIC EFFICIENCY OF OPTIMIZED GEOMETRY

the blade, that results in higher efficiencies. Furthermore, Mach number is successfully decreased during the optimization. The performance map of the radial compressor stage is shown in Fig. 24 and 25. The first figure visualizes the ratio of total and static pressure for three speed lines, starting at $n=80\%$ up to $n=100\%$. The ADP with a pressure ratio of 2.3 and a mass flow rate of $0.26 \frac{\text{kg}}{\text{s}}$ has a decent distance to the surge line, at the speed line with $n=100\%$. Without the integration of the highly throttled operating point, the optimizer would possibly shift the ADP up to the surge line. The isentropic efficiency with respect to the mass flow rate is shown in Fig. 25. It can be noticed, that the ADP is at the maximum of the speed line $n=100\%$. Furthermore, higher efficiencies are possible by reducing the rotation speed of the compressor, that leads to lower pressure ratios.

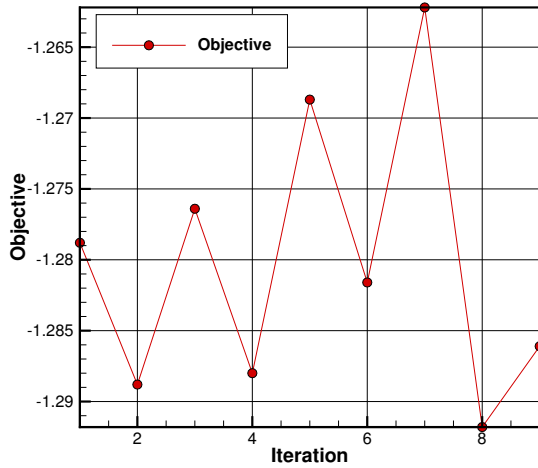


FIGURE 26: CONVERGENCE HISTORY OF AUTOMATIC HYPERPARAMETER TUNING

5. AUTOMATIC HYPERPARAMETER TUNING

The results of the comprehensive study for different infill criteria combinations shown in Fig. 14 motivate further investigation of the best choice for the values of the model parameters w_E , w_P and w_N . This is carried out by an AHPT. The hyperparameter tuning is done by an implemented Bayesian optimization approach. The optimization process is supported by a Gaussian process regression surrogate model. Due to the fact that only the ratio of w_E to w_P and w_N are influencing the performance of the optimization process, w_E , w_P and w_N can be considered in the interval $[0, 1]$ without loss of generality. The optimization process is initialized by two randomly generated samples of model parameter combinations. Further iterations are generated by evaluating the surrogate model. The result of the AHPT is shown in Fig. 26. It can be seen, that iteration eight has the lowest objective value and is more optimal than the best found solution within the comprehensive study. An objective value of -1.2918 could be achieved with model parameters $(w_E, w_P, w_N) = (0.344, 0.310, 0.346)$. The geometry modified by the AHPT is compared with the optimized geometry with infill criteria combination $(w_E, w_P, w_N) = (1, 3, 1)$. Significant changes of the circumferential coordinates, the control points of the β angle distribution and the control points of the leading edge interpolation were noted. The circumferential coordinate was further optimized by modifying #13: $60.83^\circ \rightarrow 63.00$ and #14: $60.00^\circ \rightarrow 57.99$. Slight modifications of the β angle control points #20: $0.06 \rightarrow 0.10$, #21: $0.60 \rightarrow 0.55$ and #22: $0.073 \rightarrow 0.032$ further optimized the intermediate shape of the impeller geometry. Another modification could be observed of the leading edge control points: #8: $-0.033 \rightarrow -0.076$, #9: $-0.023 \rightarrow -0.013$, #10: $0.028 \rightarrow 0.060$ and #12: $-0.10 \rightarrow 0.024$. The resulting geometry of the AHPT and the geometry with the model parameters $(w_E, w_P, w_N) = (1, 3, 1)$ is shown in Fig. 27.

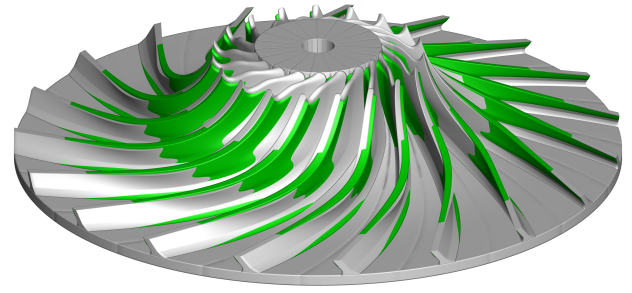


FIGURE 27: COMPARISON OF THE IMPELLER GEOMETRY OF AUTOMATIC HYPERPARAMETER TUNING AND INFILL CRITERIA COMBINATION $(w_E, w_P, w_N) = (1, 3, 1)$

6. CONCLUSION

The paper presents an aerodynamic optimization for a radial compressor stage with application in a HTHP test rig. The working fluid is water steam. The rotational speed was kept constant at 100,000 rpm.

The optimization was done by a gradient-free algorithm, that is accelerated by surrogate models. The blade and vane is parametrized by 40 free variables. A highly throttled operating point is regarded, to achieve a descent distance of the ADP to the surge line. Three different surrogate models and infill criteria were investigated. The best combination of infill criteria was found to be $(w_E, w_P, w_N) = (1, 3, 1)$ and $(w_E, w_P, w_N) = (1, 1, 3)$.

The optimized geometry satisfies all constraints. The required pressure ratio of 2.3 could be realized. An isentropic efficiency of nearly 75% in the ADP for the compressor stage was calculated. The effect of negative loading could be successfully avoided in the optimized impeller geometry.

Furthermore, an automated hyperparameter tuning was carried out to investigate the most optimal combination of infill criteria. The result was a geometry with an improved isentropic efficiency of about 0.68 percentage points compared to the result of the optimization with $(w_E, w_P, w_N) = (1, 3, 1)$.

Finally, the optimized compressor stage was analyzed in terms of aerodynamic performance. Special features, like β angle, rake angle and leading edge contour were described quantitatively. During the optimization, the leading edge parametrization reached the parameter limit. Further optimization with refined leading edge control points could generate more optimal solutions. That will be investigated in the next design steps of turbocompressors for HTHP.

ACKNOWLEDGMENTS

We would like to thank the DLR, Energy Programme Directorate for its support and the unknown reviewers for their useful

suggestions.

REFERENCES

- [1] Pörtner, H.-O. “IPCC, 2022: Summary for Policymakers.” (2022) DOI [10.1017/9781009325844.001](https://doi.org/10.1017/9781009325844.001).
- [2] Meroni, Andrea, Zühlsdorf, Benjamin, Elmegaard, Brian and Haglind, Fredrik. “Design of centrifugal compressors for heat pump systems.” *Applied Energy* Vol. 232 (2018): pp. 139–156. DOI <https://doi.org/10.1016/j.apenergy.2018.09.210>. URL <https://www.sciencedirect.com/science/article/pii/S0306261918315290>.
- [3] Schiffmann, J. “Integrated Design and Multi-objective Optimization of a Single Stage Heat-Pump Turbo-compressor.” *Journal of Turbomachinery* Vol. 137 No. 7 (2015). DOI [10.1115/1.4029123](https://doi.org/10.1115/1.4029123). URL https://asmedigitalcollection.asme.org/turbomachinery/article-pdf/137/7/071002/6301835/turbo_137_07_071002.pdf, URL <https://doi.org/10.1115/1.4029123>. 071002.
- [4] Casey, Michael and Robinson, Chris. *Radial Flow Turbo-compressors: Design, Analysis, and Applications*. Cambridge University Press (2021). DOI [10.1017/9781108241663](https://doi.org/10.1017/9781108241663).
- [5] Goinis, Georgios. “Gehäusestrukturierungen für transsonische Verdichter.” Technical report no. Ruhr-Universität Bochum. 2020. URL <https://elib.dlr.de/140455/>.
- [6] Raitor, Till, Reutter, Oliver, Aulich, Marcel and Nicke, Eberhard. “Aerodynamic Design Studies of a Transonic Centrifugal Compressor Impeller Based on Automatic 3D-CFD Optimization.” *10th European Turbomachinery Conference*. 2013. URL <https://elib.dlr.de/85592/>.
- [7] Cumpsty, N.A. *Compressor Aerodynamics*. No. Bd. 10 in *Compressor aerodynamics*, Krieger Pub. (2004).
- [8] Ratz, Johannes, Leichtfuß, Sebastian, Beck, Maximilian, Schiffer, Heinz-Peter and Fröhlig, Friedrich. “Surge Margin Optimization of Centrifugal Compressors Using a New Objective Function Based on Local Flow Parameters.” *International Journal of Turbomachinery, Propulsion and Power* Vol. 4 No. 4 (2019). DOI [10.3390/ijtp4040042](https://doi.org/10.3390/ijtp4040042). URL <https://www.mdpi.com/2504-186X/4/4/42>.
- [9] den Braembussche, Van. “Optimization of Radial Impeller Geometry.” 2006.
- [10] Hiradate, Kiyotaka, Kannno, Toshio, Nishida, Hideo, Shinkawa, Yasushi and jyoukou, Satoshi. “1210 Improvement in Efficiency and Operating Range of Centrifugal Blower Stage for Sewage Aeration Blower.” *The Proceedings of the Fluids engineering conference* Vol. 2010 (2010): pp. 345–346. DOI [10.1299/jsmefed.2010.345](https://doi.org/10.1299/jsmefed.2010.345).
- [11] Châtel, Arnaud and Verstraete, Tom. “Aerodynamic Optimization of the SRV2 Radial Compressor Using an Adjoint-Based Optimization Method.” Vol. Volume 10D: Turbomachinery — Multidisciplinary Design Approaches, Optimization, and Uncertainty Quantification; Turbomachinery General Interest; Unsteady Flows in Turbomachinery (2022). DOI [10.1115/GT2022-82530](https://doi.org/10.1115/GT2022-82530). URL <https://asmedigitalcollection.asme.org/GT/proceedings-pdf/GT2022/86120/V10DT34A014/6937244/v10dt34a014-gt2022-82530.pdf>, URL <https://doi.org/10.1115/GT2022-82530>. V10DT34A014.
- [12] Voß, Christian, Aulich, Marcel and Raitor, Till. “Metamodel Assisted Aeromechanical Optimization of a Transonic Centrifugal Compressor.” *1st TRACE User Conference*. 2014. URL <https://elib.dlr.de/90969/>.
- [13] Aulich, Marcel, Voß, Christian and Raitor, Till. “Optimization Strategies demonstrated on a Transonic Centrifugal Compressor.” 2014.
- [14] Hottot, Romain, Châtel, Arnaud, Coussement, Gregory, Debruyne, Tom and Verstraete, Tom. “Comparing Gradient-Free and Gradient-Based Multi-Objective Optimization Methodologies on the VKI-LS89 Turbine Vane Test Case.” *Journal of Turbomachinery* Vol. 145 No. 3 (2022). DOI [10.1115/1.4055577](https://doi.org/10.1115/1.4055577). URL https://asmedigitalcollection.asme.org/turbomachinery/article-pdf/145/3/031001/6928070/turbo_145_3_031001.pdf, URL <https://doi.org/10.1115/1.4055577>. 031001.
- [15] Hehn, Alexander, Mosdzien, Moritz, Grates, Daniel and Jeschke, Peter. “Aerodynamic Optimization of a Transonic Centrifugal Compressor by Using Arbitrary Blade Surfaces.” *Journal of Turbomachinery* Vol. 140 No. 5 (2018). DOI [10.1115/1.4038908](https://doi.org/10.1115/1.4038908). URL https://asmedigitalcollection.asme.org/turbomachinery/article-pdf/140/5/051011/6308811/turbo_140_05_051011.pdf, URL <https://doi.org/10.1115/1.4038908>. 051011.
- [16] Aissa, Mohamed H. and Verstraete, Tom. “Metamodel-Assisted Multidisciplinary Design Optimization of a Radial Compressor.” *International Journal of Turbomachinery, Propulsion and Power* Vol. 4 No. 4 (2019). DOI [10.3390/ijtp4040035](https://doi.org/10.3390/ijtp4040035). URL <https://www.mdpi.com/2504-186X/4/4/35>.
- [17] Schmitz, Andreas. “Multifidelity-Optimierungsverfahren für Turbomaschinen.” Technical report no. Ruhr Universität Bochum. 2020. URL <https://elib.dlr.de/140674/>.
- [18] Martinetz, Thomas and Schulten, K. “A “Neural-Gas” Network Learns Topologies.” *Artificial neural networks* Vol. 1 (1991): pp. 397–402.
- [19] Voß, Christian and Nicke, Eberhard. “Automatische Optimierung von Verdichterstufen.” *Technische Informationsbibliothek Hannover* (2008).
- [20] Drela, Mark and Youngren, Harold. “A User’s Guide to MISES 2.63.” Version 2.63. MIT Aerospace Computational Design Laboratory (2008). Accessed December 20, 2022, URL <https://web.mit.edu/drela/Public/web/mises/mises.pdf>.
- [21] Sauer, M. “An optimization based approach to multi-block structured grid generation.” *6th European Conference on Computational Mechanics* (11-15 June 2018, Glasgow, UK).
- [22] Slater, John W. “Examining Spatial (Grid) Convergence.” Version 1.0. National Aeronautics and Space Administration (2022). Accessed November 29, 2022, URL <https://www.grc.nasa.gov/WWW/wind/valid/tutorial/spatconv.html>.

- [23] Roache, P. J. “Perspective: A Method for Uniform Reporting of Grid Refinement Studies.” *Journal of Fluids Engineering* Vol. 116 No. 3 (1994): pp. 405–413. DOI [10.1115/1.2910291](https://doi.org/10.1115/1.2910291). URL https://asmedigitalcollection.asme.org/fluidsengineering/article-pdf/116/3/405/5531128/405_1.pdf, URL <https://doi.org/10.1115/1.2910291>.
- [24] Franke, Martin, Kügeler, Edmund and Nürnberger, Dirk. “Das DLR-Verfahren TRACE: Moderne Simulationstechniken für Turbomaschinenströmungen.” DGLR (ed.). *Deutscher Luft- und Raumfahrtkongress 2005*. 2005.
- [25] Dhondt, Guido. “CalculiX - A Free Software Three-Dimensional Structural Finite Element Program.” Version 2.19 (2022). Accessed Dezember 1, 2022, URL <http://www.calculix.de/>.